Phanisri P. Pratapa[1]
Department of Civil Engineering,
Indian Institute of Technology Madras,
Chennai, TN 600036, India
e-mail: ppratapa@iitm.ac.in

Ke Liu
Department of Mechanical and Civil Engineering,
California Institute of Technology,
Pasadena, CA 91125
e-mail: liuke@caltech.edu

Siva P. Vasudevan
Department of Civil Engineering,
Indian Institute of Technology Madras,
Chennai, TN 600036, India
e-mail: ce19d750@smail.iitm.ac.in

Glaucio H. Paulino
School of Civil and Environmental Engineering,
Georgia Institute of Technology,
Atlanta, GA 30332
e-mail: paulino@gatech.edu

Reprogrammable Kinematic Branches in Tessellated Origami Structures

We analyze the folding kinematics of a recently proposed origami-based tessellated structure called the Morph pattern, using thin, rigid panel assumptions. We discuss the geometry of the Morph unit cell that can exist in two characteristic modes differing in the mountain/valley assignment of a degree-four vertex and explain how a single tessellation of the Morph structure can undergo morphing through rigid origami kinematics resulting in multiple hybrid states. We describe the kinematics of the tessellated Morph pattern through multiple branches, each path leading to different sets of hybrid states. We study the kinematics of the tessellated structure through local and global Poisson's ratios and derive an analytical condition for which the global ratio switches between negative and positive values. We show that the interplay between the local and global kinematics results in folding deformations in which the hybrid states are either locked in their current modes or are transformable to other modes of the kinematic branches, leading to a reprogrammable morphing behavior of the system. Finally, using a bar-and-hinge model-based numerical framework, we simulate the nonlinear folding behavior of the hybrid systems and verify the deformation characteristics that are predicted analytically. [DOI: 10.1115/1.4049949]

Keywords: folding and origami

1 Introduction

Origami patterns have attracted substantial attention in recent years due to a wide array of potential applications, such as those involving metamaterials [1–6] and structures [7–11]. Origami patterns such as standard Miura-ori [12,13] and standard Eggbox [14,15] have been extensively studied in the research community as they are some of the simplest tessellations with degree-four vertices [16,17] characterized by three mountains and one valley, and four mountain creases, respectively. A notable feature of these and many other origami patterns is that, as they fold between their extreme geometric states, the crease topologies (i.e., the mountain/valley assignments) remain fixed. In this paper, we discuss characteristics of a degree-four *Morph* origami pattern recently proposed by the authors [18], which exhibits topological morphing by switching one of its creases between mountain and valley.

The standard Miura-ori and standard Eggbox patterns gained wide attention of scientists and engineers from many fields due to their ability to display geometrically dependent and tunable negative and positive Poisson's ratios, respectively [15]. Interestingly, it was shown that the Morph pattern can exhibit a Poisson's ratio from negative infinity to positive infinity as it undergoes topological morphing between a Miura mode (which is topologically similar to a standard Miura-ori) and an Eggbox mode (which is topologically similar to a standard Eggbox pattern). In addition, the standard Miura-ori and Eggbox patterns can be derived as particular cases within the design space of the Morph pattern. The Poisson's ratio switching phenomenon has also been recently observed in other systems [19–21] including some origami metamaterials [22–24].

In this paper, we study various kinematic aspects of the Morph origami system, for application to reprogrammable metamaterials. We distinguish between the Morph unit cell and the Morph pattern. The Morph unit cell has two characteristic modes called the Miura and the Eggbox modes and has a relatively simple kinematic behavior. However, the Morph pattern (tessellation) is an assemblage of the Morph unit cells which, when coupled with the possibility of topological morphing, exhibits a rich and complex kinematic behavior. Therefore, we dedicate most of this paper to exploring and explaining the resulting interesting features of the Morph pattern. Specifically, we focus on the kinematics of *hybrid states* which are inter-transformable geometric configurations that can be obtained from the Morph pattern. Throughout this paper, we assume that the panels are thin and rigid, unless specified otherwise.

Contrasting the previous work on the Morph concept [18], the novelty of the current paper is highlighted as follows. (i) We explain the rigid origami kinematics of the Morph pattern through intersection of compatibility and configuration curves. Using this approach, we explain the inter-transformability between various states of the Morph pattern which renders the system to exhibit reprogrammable kinematic branches. (ii) Unlike the framework used in Ref. [18], which presented a basic branching case, we provide a representation of the configuration path of the Morph pattern that can distinguish between various sets of hybrid states. This allows for exploration of the rich features of the Morph pattern's kinematic branches. (iii) We derive the analytical condition for the Poisson's ratio sign switching in the Morph pattern that can be directly used to program the system to display the desired switching. (iv) We explain the detailed mechanism for mode-locking behavior mathematically, based on the interplay of local-global kinematics, and verify this behavior through numerical simulations using a bar-and-hinge model [25].

This paper is organized as follows. We first review the geometry, configuration path, and kinematics of the Morph unit cell. Next, we explain the construction of the Morph pattern in both its uniform and hybrid states, which contain identical and non-identical unit cells respectively. Afterwards, we explain the rigid kinematics and transformations among various states, provide a new approach to represent configuration paths, and describe the kinematics of the Morph pattern. We verify the theoretical predictions using numerical simulations. Finally, we summarize the work and discuss directions for future research.

[1]Corresponding author.

Contributed by Mechanisms and Robotics Committee of ASME for publication in the Journal of Mechanisms and Robotics. Manuscript received September 27, 2020; final manuscript received January 18, 2021; published online March 12, 2021. Assoc. Editor: Philip A. Voglewede.

2 The Morph Unit Cell

A degree-four origami vertex consists of four creases and four panels intersecting at a vertex [16]. The Morph unit cell is a special case of the general degree-four vertex with the design space given by $\alpha>0$, $\beta>0$ and $\alpha+\beta\leq\pi$, where α, β are the angles of the parallelogram-shaped panels. Clearly, the standard Miura-ori, given by $\alpha+\beta=\pi$, and the standard Eggbox, given by $\beta=\alpha$, are special cases of the Morph vertex. In this section, we describe the geometry of the Morph unit cell and summarize its configuration path and its kinematics. We use the understanding from this section as a stepping stone to explain the formation of the Morph pattern and its unique characteristics.

2.1 Geometry of the Morph Unit Cell. The geometry of the Morph unit cell is shown in Fig. 1. It is a single degree-of-freedom system[2] whose folded state can be expressed by any of the folding angles ϕ, ψ, or the dihedral angles between the panels γ_1, γ_2, γ_3, and γ_4. The vertices are indexed as O_i where $i=1$ to 9. The most defining feature of the Morph unit cell is its ability to change the crease topology, which is given by the mountain/valley assignment. Without loss of generality, when we assume $\beta<\alpha$ and $\alpha+\beta<\pi$, the creases O_5O_2, O_5O_4, O_5O_8 remain as mountains and the crease O_5O_6 (highlighted in Fig. 1) can switch to being either a valley or a mountain depending on whether γ_3 is greater than or less than π. Correspondingly, the Morph unit cell exists in two characteristic modes which we call the Miura and the Eggbox modes, as the crease topologies of these modes are same as the standard Miura-ori and the standard Eggbox unit cells, respectively. When $\beta<\alpha$ and $\alpha+\beta<\pi$, the unit cell vertex is non-developable and therefore is a generalization of the standard Eggbox pattern, which exhibits two flat-folded states that are topologically similar. However, the two flat-folded states of the Morph unit cell are distinct as one of them occurs in the Miura mode with $\phi=\phi_{min}=\alpha-\beta$, whereas the other occurs in the Eggbox mode with $\phi=\phi_{max}=\alpha+\beta$. The unit cell dimensions (W, L) can be derived in terms of the panel dimensions a, b, c, and the folding angles. We constrain $b=a|\cos\alpha/\cos\beta|$ in order to ensure the orthorhombic nature of the unit cell.

2.2 Configuration Path of the Morph Unit Cell. The parameter space that describes the geometric configuration of the Morph unit cell can be given by the set of all points $\{\phi,\psi\}\in\mathcal{Q}:[\phi_{min},\phi_{max}]\times[0,\psi_{max}]$, where the angles ϕ and ψ represent the folding angles between opposite creases of the degree-four Morph vertex and ψ_{max} represents the upper bound of ψ. We note that the two folding angle parameters are not independent due to the presence of rigid panels between the creases. The constraining relation between them can be derived using concepts of spherical trigonometry [27] about vertex O_5 and is given by

$$\psi=f(\phi)=\cos^{-1}\left[\cos 2\alpha+\frac{2(\cos\beta-\cos\alpha\cos\phi)^2}{\sin^2\phi}\right] \quad (1)$$

We define the configuration path [28] of the Morph unit cell as the continuous curve in the parameter space that describes the folding mechanism. In other words, the configuration path represents the set of all geometric configurations of the unit cell while it undergoes folding and is directly related to the kinematics of the system. Equation (1) represents the configuration path of the Morph unit cell. This is plotted for $\alpha=60$ deg and $\beta=40$ deg in Fig. 2 as dashed and solid curves for Miura and Eggbox modes, respectively. The curve clearly distinguishes the two characteristic modes in the configuration path and indicates that the transition between Miura and Eggbox modes happens when $\psi=\psi_{max}=2\beta$. This is the point when the crease O_5O_6 is co-planar with the two adjacent panels and is about to switch the mountain/valley assignment. Figure 3 shows the physical model of a Morph unit cell in various configurations.

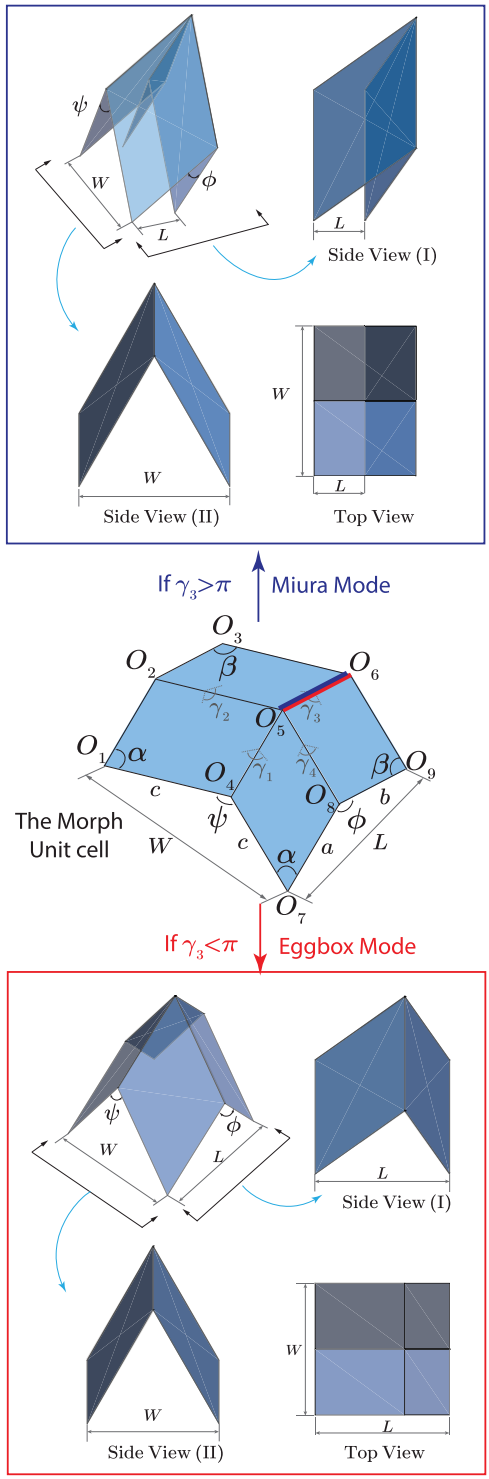

Fig. 1 The two characteristic modes of the Morph unit cell: Miura mode and Eggbox mode

2.3 Kinematics of the Morph Unit Cell. The kinematics of the Morph unit cell can be completely described using Eq. (1). The local Poisson's ratio for the unit cell characterizes the

[2]This can be easily verified using the modified Grübler–Kutzbach criterion for spherical linkages [26]. The Morph unit cell has four panels (rigid links) and four creases (revolute joints) leading to a mobility of 1.

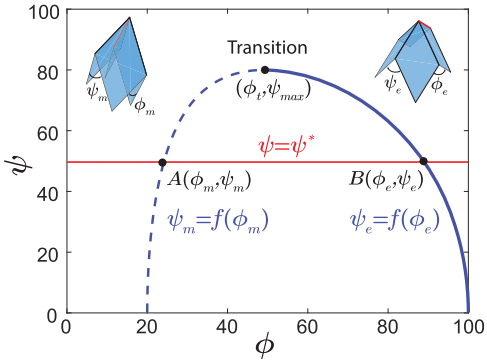

Fig. 2 Configuration path of a Morph unit cell in terms of the folding angles. The Miura mode cells are represented by point *A* and the Eggbox mode cells are represented by point *B* which lie on the dashed and solid curves, respectively.

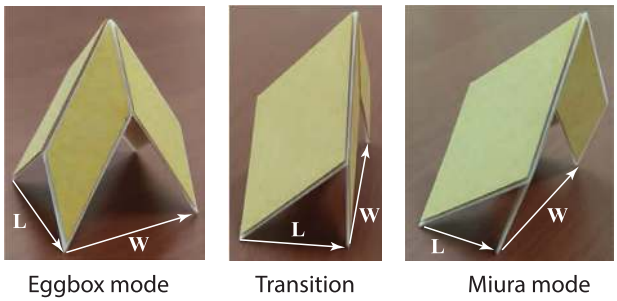

Fig. 3 Physical model of the Morph unit cell

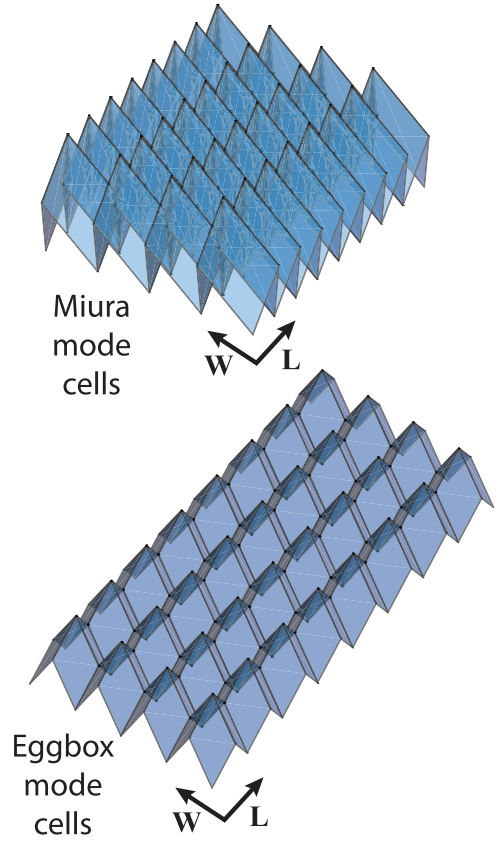

Fig. 4 Tessellation of the Morph unit cells in Miura and Eggbox modes to form uniform Morph patterns

deformation behavior and is given by

$$\nu_l = -\frac{dW/W}{dL/L} = -\frac{dW/d\psi}{dL/d\phi}\frac{L}{W}\frac{d\psi}{d\phi} = \left[\frac{\cos^2\alpha+\cos^2\beta-2|\cos\alpha\cos\beta|\cos\phi}{\sin^2(\psi/2)|\cos\alpha\cos\beta|}\right]\left[\frac{(\cos\beta-\cos\alpha\cos\phi)(\cos\alpha-\cos\beta\cos\phi)}{\sin^4\phi}\right] \quad (2)$$

Clearly, Poisson's ratio depends only on the geometry of the unit cell defined in terms of α, β, ϕ, and ψ. The term $(\cos\alpha-\cos\beta\cos\phi)$ in the expression for ν_l dictates its sign and it can be shown that this term is negative for the Miura mode and positive for the Eggbox mode as it is directly proportional to cos $(\gamma_3/2)$. In addition, the sin $^2(\psi/2)$ term in the denominator leads to singularities in the flat-folded states giving rise to $-\infty$ and $+\infty$ Poisson's ratios as $\psi \to 0$ in the Miura and Eggbox modes, respectively. Poisson's ratio switches sign smoothly about $\nu_l = 0$ when $(\cos\alpha-\cos\beta\cos\phi)=0$ as $\gamma_3=\pi$ (transition state).

3 The Morph Pattern

The equivalence between the triangles $\Delta O_1O_2O_3$ ($\Delta O_1O_4O_7$) and $\Delta O_7O_8O_9$ ($\Delta O_3O_6O_9$) allows for replication along the **W** (**L**) direction by placing identical Morph unit cells adjacent to each other. The tessellation of identical Morph unit cells in either of its characteristic modes, along the two orthogonal directions shown in Fig. 4 leads to the uniform Morph pattern. The Morph pattern also allows for the existence of hybrid states that may or may not have such translation symmetry, which typically does exist in common origami patterns. These hybrid states are obtained by combining the two (non-identical) characteristic modes of the Morph unit cell with compatible geometries (see Fig. 5). This feature allows for a rich set of hybrid states associated with various combinations of the two modes that include both periodic and non-periodic patterns.

In this section, we first describe the geometry of the Morph pattern. We then explain the transformability of the uniform Morph pattern into its hybrid states and characterize the configuration paths of the Morph pattern. Finally, we discuss the kinematics of the Morph pattern.

3.1 Geometry of the Morph Pattern. The geometry of the Morph pattern (including its hybrid states) is characterized by the folding angles (ϕ, ψ) of each of the individual unit cells. Note that ψ is the angle between the opposite mountain creases of the degree-four Morph vertex, and ϕ is the angle between the other set of opposite creases, one of which can switch between being a mountain or a valley (see Fig. 1). For a Morph pattern in an arbitrary hybrid state, some of the unit cells could be in the Miura mode and the rest of them could be in the Eggbox mode. We will denote the folding angles for the unit cells in Miura mode to be ϕ_m, ψ_m and those in Eggbox mode to be ϕ_e, ψ_e. Similarly, we will denote the unit cell dimensions as L_m, W_m and L_e, W_e, respectively, for the Miura and Eggbox modes. In both modes, we have,

$$\psi_m = f(\phi_m), \quad \psi_e = f(\phi_e) \quad (3)$$

where f is the function defined in Eq. (1). Additionally, for both modes to co-exist in the same pattern by tessellating along the **L** direction, we also need the compatibility condition

$$\psi_m = \psi_e = \psi^* \quad (4)$$

The above Eqs. (3) and (4), determine the folding angles of each of the unit cells in any hybrid state of the Morph pattern, as the points

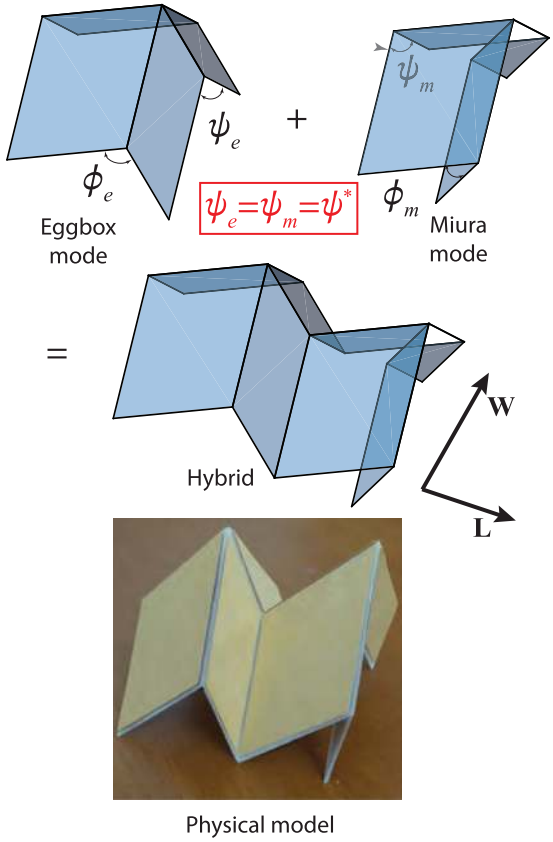

Fig. 5 Combining compatible unit cells in Miura and Eggbox modes to form a hybrid state

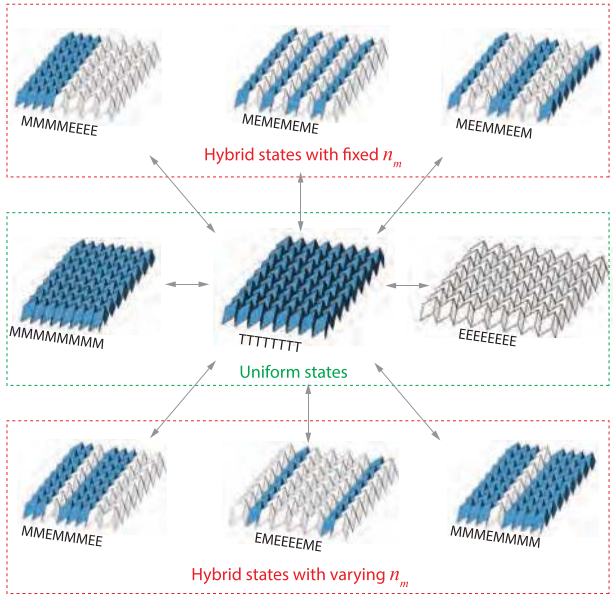

Fig. 6 Realizations of the Morph pattern with 8 × 8 cells—the three uniform states and sample hybrid states. The double arrows indicate inter-transformability between states. *M*, *E*, *T* represent the strips in Miura mode, Eggbox mode, and Transition state, respectively. The parameter n_m is the number of strips in the Miura mode. The strips in the Eggbox mode are shown in white color.

of intersection (A, B in Fig. 2) between the curve $\psi = f(\phi)$ and the straight line $\psi = \psi^*$. It can be shown that

$$\phi_m = \cos^{-1}\left(\frac{\cos\alpha}{\cos(\psi^*/2)}\right) - \cos^{-1}\left(\frac{\cos\beta}{\cos(\psi^*/2)}\right) \tag{5}$$

$$\phi_e = \cos^{-1}\left(\frac{\cos\alpha}{\cos(\psi^*/2)}\right) + \cos^{-1}\left(\frac{\cos\beta}{\cos(\psi^*/2)}\right) \tag{6}$$

Further description of the geometry of the Morph pattern, especially for the hybrid states, can be provided by the type of arrangement of the non-identical unit cells. The unit cells that are tessellated along the **W** direction are all identical at all folding angles and therefore form a strip of uniform cells which are either in the Miura mode or the Eggbox mode which we shall denote as M and E, respectively. On the other hand, the unit cells tessellated along the **L** direction need not be identical except that they all have the same angle $\psi = \psi_m = \psi_e = \psi^*$ and can have different $\phi = \phi_m$ or $\phi = \phi_e$, where $\phi_m \neq \phi_e$. Now different hybrid state geometries can be denoted by how the strips of cells are arranged: *MMMMEEEE*, *MEMEMEME*, *MEEMEEM*, *MMEMMMEE* etc., as shown in Fig. 6. Using this notation, the uniformly tessellated Morph pattern is denoted as either *MMMMM…*, *EEEEE…* or *TTTTT…* depending on whether all the unit cells are in Miura mode, Eggbox mode, or the transition state, respectively.

3.2 Hybrid States Through Rigid Folding Kinematics. One of the fascinating features of the Morph pattern is that all the hybrid states of the Morph pattern including the uniformly tessellated states are inter-transformable through rigid origami kinematics. This can be theoretically understood as follows. First, we will show that any hybrid state pattern can be transformed to a uniform transition state through rigid kinematics. Next, we will describe how starting from a uniform transition state, any hybrid state with arbitrary strip arrangement can be obtained through rigid origami folding. By combining these two steps, we show transformability between all the states of the Morph pattern via the transition state is possible.

Consider a hybrid state with an arbitrary strip arrangement and the folded state of the unit cells given by (ϕ_m, ϕ_e, ψ^*) represented by the two points A, B in Fig. 2. As we smoothly change the folded state of the system while staying on the curve $\psi = f(\phi)$, kinematic compatibility holds and, therefore, each individual unit cell undergoes rigid folding. This rigid folding causes ψ^* to either decrease or increase, i.e., the line $\psi = \psi^*$ in Fig. 2 moves down or up, respectively. If ψ^* decreases toward zero, $\phi_m \to \phi_{min}$ and $\phi_e \to \phi_{max}$ and the strip arrangement is conserved. However, if ψ^* increases toward ψ_{max}, $\phi_m \to \phi_t$, and $\phi_e \to \phi_t$ and the system transforms into the uniform Morph pattern with all unit cells reaching the transition state. At this state, the line $\psi = \psi^*$ intersects the curve $\psi = f(\phi)$ at only one point (ϕ_t,$\psi_{\max}$).

Further folding from the transition state with identical unit cells is possible only through reduction of ψ^*. However, this can happen either by decreasing or by increasing angle ϕ of each of the unit cells according to which they assume Miura or Eggbox modes, respectively. By controlling the switching of the strips between the Miura and Eggbox modes, one can obtain various other hybrid states. We note that a detailed discussion concerning how one could control [29] the switching between different types of strips is beyond the scope of this paper.

Therefore, inter-transformability between all the hybrid states and the uniform states is feasible by rigid folding them to the transition state and then switching the strip arrangement to a different desired configuration. This is demonstrated schematically in Fig. 6 for some of the states.

3.3 Configuration Paths of the Morph Pattern. Unlike the configuration path of the Morph unit cell which has only two branches—one on either side of the transition point (see Fig. 2), the Morph pattern has multiple additional branches to describe the folding of hybrid states. We have described the parameter space of the Morph unit cell in terms of the folding angles ϕ and

ψ. However, representing the parameter space of the Morph pattern in terms of folding angles alone over simplifies the space and cannot distinguish between various paths arising due to the hybrid states [18]. To overcome this issue, we choose the parameter space of the Morph pattern as the set of all points $\{\psi, L'\} \in \mathcal{Q}'$:$[0, \psi_{max}] \times [L'_{min}, L'_{max}]$, where $\psi(=\psi^*)$ is the folding angle that is common across all the modes, and L' is the total pattern length along the **L** direction, bounded by L'_{min}, L'_{max}. The expression for L' is given by

$$L' = n_m L_m(\phi_m) + n_e L_e(\phi_e) \tag{7}$$

where L_m, L_e are the Morph unit cell lengths in Miura, Eggbox modes, respectively, and n_m, n_e are the number of strips in Miura, Eggbox modes, respectively. For any given choice of n_m, n_e, the configuration path of the system in the parameter space can be identified by using Eqs. (5), (6) in Eq. (7). Therefore, using this approach we can distinguish between various configuration paths associated with the hybrid states as shown in Fig. 7.

In Fig. 7, the total number of strips in the Morph pattern, given by $n = n_m + n_e$, is fixed to be 6 and we vary the number of Miura mode strips across various paths shown in the figure. The top and bottom paths with $n_m = 0$ and $n_m = 6$ correspond to the uniform patterns. Since $L_m < L_e$, the overall length L' of the hybrid states decreases with the increase in the number of Miura mode strips, at any given ψ. As described in Sec. 3.2, the transformation between various states happens by traversing along these paths via the transition point denoted by *TTTTTT* in the figure. In this context, we call this intersection point, the kinematic bifurcation point [18]. Since all the paths pass through a common point, we refer to these paths as kinematic branches [30].

We note that the above-mentioned approach to distinguish configuration paths of various hybrid states cannot separate degenerate states that may exist along each path. For example, the path represented by $n_m = 1$ in Fig. 7 is identical for all the hybrid states *MEEEEE*, *EMEEEE*, *EEMEEE*, *EEEMEE*, *EEEEME*, and *EEEEEM*. However, as we will see in Sec. 3.4, the geometric mechanics of the hybrid states are in general only governed by n_m for a given n and not by the degenerate arrangement of the strips.

3.4 Kinematics of the Morph Pattern. We have seen in Sec. 3.3 that the Morph unit cell can exhibit negative or positive Poisson's ratio depending on whether it is in the Miura mode or the Eggbox mode. By virtue of rigid body kinematics, the uniform patterns obtained by tessellating either the Miura or the Eggbox mode cells will behave in a manner similar to that of the corresponding single unit cell. However, the hybrid states which are a combination of both Miura and Eggbox mode unit cells exhibit complex deformation behavior due to the interplay between the local and global kinematics. As we will see below, this leads to some very interesting properties.

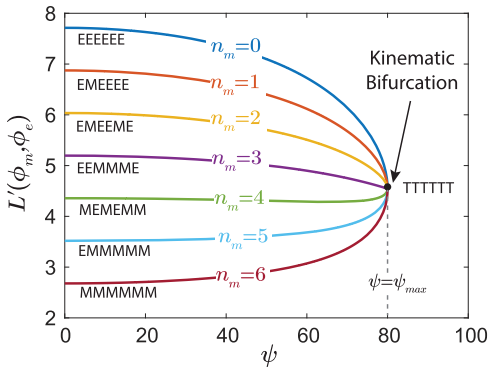

Fig. 7 Kinematic branches of the Morph pattern. *EEEEEE*, *MMMMMM*, *TTTTTT* are uniform states and the rest are hybrid states. The parameter n_m denotes the number of strips in the Miura mode. The panel geometry was chosen as $\alpha = 60$ deg, $\beta = 40$ deg, and $a = 1$.

We define the global stretching Poisson's ratio of a Morph pattern as the ratio of infinitesimal strains in both the tessellation directions which is given by

$$\nu_g = -\frac{dL'/L'}{dW'/W'} \tag{8}$$

where L' is given by Eq. (7) and W' is the total width of each of the strips and is equal to nW for strips with n unit cells. Using Eqs. (5)–(8), we can derive the following expression for the global Poisson's ratio of the Morph pattern for any arbitrary hybrid state parameterized by n_m, n_e.

$$\nu_g = p(\psi)q(\psi) \tag{9}$$

where

$$p(\psi) = \frac{ab\sin^2\frac{\psi}{2}}{L'\cos^3\frac{\psi}{2}} \tag{10}$$

and

$$q(\psi) = \left[\frac{\cos\alpha}{\sin((\phi_e+\phi_m)/2)}\left(\frac{n_e\sin\phi_e}{L_e}+\frac{n_m\sin\phi_m}{L_m}\right) + \frac{\cos\beta}{\sin((\phi_e-\phi_m)/2)}\left(\frac{n_e\sin\phi_e}{L_e}-\frac{n_m\sin\phi_m}{L_m}\right)\right] \tag{11}$$

For a fixed number of strips n, the local contributions from the unit cells of contrasting modes affect the global Poisson's ratio through the parameters n_m, n_e. Clearly, the above expression for the global Poisson's ratio does not depend on the arrangement of degenerate strips. For example, *EEMMEE* and *EEEMEM* will have the same ν_g.

One interesting feature that develops due to the local-global interplay is that unlike the Morph unit cell or the uniform Morph pattern in which the zero Poisson's ratio and the change of sign of Poisson's ratio occurs at the transition state, the hybrid states can exhibit this behavior when they are away from a transition state (i.e., $\phi_e \neq \phi_m$). To derive this condition, we set[3] $q(\psi) = 0$ in Eq. (11). Assuming $\phi_e \neq \phi_m$, and using the relation[4] $L_m \sin\phi_e = L_e \sin\phi_m$, we get

$$\eta = \frac{\cos\beta\,\sin((\phi_e+\phi_m)/2) + \cos\alpha\,\sin((\phi_e-\phi_m)/2)}{\cos\beta\,\sin((\phi_e+\phi_m)/2) - \cos\alpha\,\sin((\phi_e-\phi_m)/2)} \tag{12}$$

where η is the ratio n_m/n_e for which Poisson's ratio sign switching can happen. The folding angle at which Poisson's ratio of the hybrid state changes sign is given by ϕ_e (or ϕ_m) that satisfies the above equation, for a given η. This angle is also related to some $\psi = \psi_s$ through Eqs. (5) and (6). For a given choice of panel geometry, the range of η values at various folding angles can be determined from Eq. (12). Figure 8(*a*) shows the relation between η and the folding angle ψ_s that satisfies Eq. (12) for various choices of α and β. It can be seen from the figure that the lowest value of η across different panel geometries is just greater than 1. This can be understood since $\alpha > \beta$, and $\phi_e > \phi_m$, then we have from Eq. (12) that $\eta > 1$. Figure 8(*a*) also indicates that the sign change of Poisson's ratio will happen at folding angles closer to the transition state ($\psi = 2\beta$) when η is closer to 1 (i.e., number of Miura mode cells is similar to the number of Eggbox mode cells). As η value increases (i.e., number of Miura mode cells dominates), the switching occurs at folding angles that gradually shift toward the flat-folded configuration ($\psi = 0$).

It is important to note that not all hybrid states of a Morph pattern (given α, β, and n) can display Poisson's ratio switching behavior

[3]Note that, although setting $p(\psi) = 0$ in Eq. (10) also leads to $\nu_g = 0$, it does not correspond to switching the sign of Poisson's ratio.

[4]This can be proved by applying sine rule for the triangle $\Delta O_7 O_8 O_9$ in the Eggbox and Miura modes.

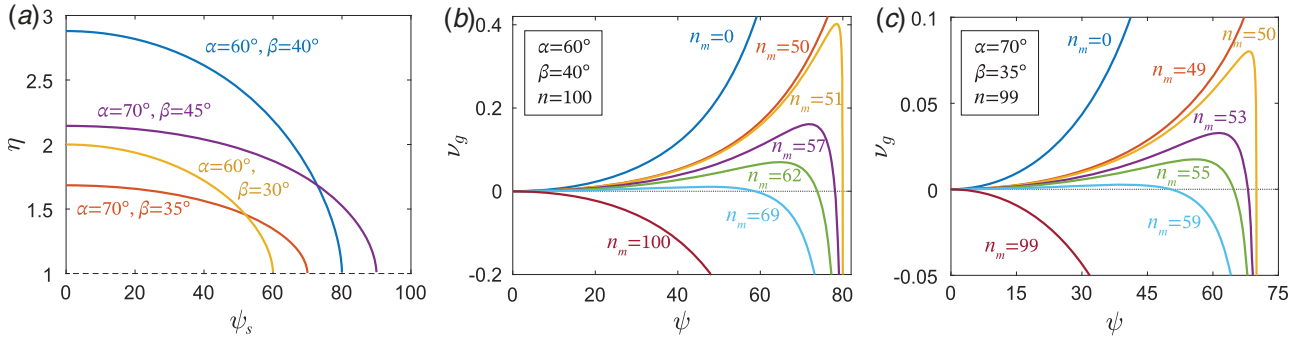

Fig. 8 (*a*) Range of η values that exhibit Poisson's ratio switching and the corresponding folding angles ψ_s at which the switch happens, for various panel geometries. (*b*), (*c*) Variation of Poisson's ratio of the hybrid states of the Morph pattern with respect to the folding angle ψ. The switching of Poisson's ratio between positive and negative values happens in the range (*b*) $51 \le n_m \le 74$~$(74/26 < \eta_{max} \approx 2.88)$ in, and in the (*c*) range $50 \le n_m \le 62$~$(62/37 < \eta_{max} \approx 1.68)$.

(see Figs. 8(*b*) and 8(*c*)). Further, it is also not necessary that there exists a hybrid state for a given Morph pattern that can exhibit Poisson's ratio switching. For example, consider a Morph pattern with $\alpha = 60$ deg and $\beta = 40$ deg. If the pattern has $n = 2$ strips, then it can never have hybrid states with a ratio n_m/n_e that is greater than 1, and therefore cannot exhibit Poisson's ratio switching. Instead, if the pattern has $n = 4$ strips, it can have $n_m/n_e = 3/1 > 1$, but it still cannot display the switching behavior as the ratio is not within the required η range for this choice of panel geometry, which is $1 < \eta < 2.88$ (see Fig. 8(*a*)). However, such a pattern with $n = 3$ can exhibit switching for $n_m/n_e = 2/1$.

Assuming that we are considering the feasible range of η, the smallest obtainable value of the ratio η corresponds to $n_m = (n/2) + 1$, if n is even (see Fig. 8(*b*)), and $n_m = (n+1)/2$, if n is odd (see Fig. 8(*c*)). On the other hand, the largest obtainable value of η is determined such that it is less than η_{max}, the theoretical maximum calculated from Eq. (12) that depends on the choice of panel angles, as shown in Fig. 8(*a*). Equation (12), along with the constraint $n_m + n_e = n$ for a given n, can be used to design the hybrid Morph pattern for tunable switching of Poisson's ratio at different ψ, as shown in Fig. 8.

Another feature of the hybrid states that develops due the local-global interplay is the presence of locked/transformable states during extension/contraction of the pattern. In this context, we refer to the hybrid patterns folding toward the nearest flat-folded state in the configuration path as *locked* states as the unit cells remain in their respective modes without any transformation. This behavior was referred to as *mode-locking* in Ref. [18]. On the other hand, we refer to the hybrid patterns with all the unit cells unfolding toward the transition state as *transformable* states as

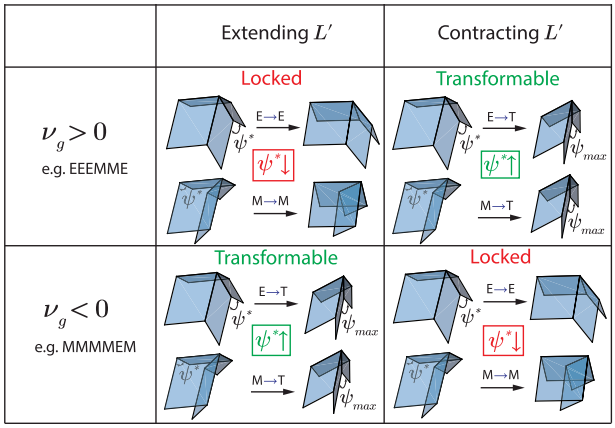

Fig. 9 Mode-locking and transformability of the hybrid states of the Morph pattern under deformation

this allows potential switching between modes. As shown in Fig. 9, such locking or transformability can occur in both the deformations—extension or contraction, depending on the sign of the global Poisson's ratio of the hybrid pattern.

This behavior can be explained based on the unit cell (local) kinematics as follows. From Fig. 2, it is clear that when ψ^* decreases, all the unit cells remain in their respective modes and eventually fold toward their flat-folded configurations. This is also related to the local Poisson's ratio ν_l by which, decreasing ψ^* will lock the topology of the respective modes. Whereas, when ψ^* increases, all the unit cells unfold toward the transition state and become identical to each other. If $\nu_g > 0$, extension along the L' dimension of the hybrid pattern causes contraction along W' dimension which requires a decrease in ψ^* and, therefore, as explained above, the unit cells are locked in their respective modes. If $\nu_g < 0$, extension along L' dimension of the hybrid pattern causes extension along W' dimension as well which requires an increase in ψ^* that takes the unit cells toward the transition state that allows mode transformation. Using similar arguments, contraction along the L' dimension of the hybrid pattern leads to transformable and locked states, when ν_g is positive and negative, respectively. To summarize in mathematical terms, if the pattern in any given configuration undergoes a folding motion with respect to a pseudo-time variable t, the modes are locked if $(d\psi^*/dt) < 0$ throughout the motion, and are transformable otherwise. Using Eq. (8), the situations that lead to locking are given by

$$\nu_g(t) > 0 \text{ and } dL'/dt > 0 \Rightarrow dW'/dt < 0 \Rightarrow d\psi^*/dt < 0 \tag{13}$$

$$\nu_g(t) < 0 \text{ and } dL'/dt < 0 \Rightarrow dW'/dt < 0 \Rightarrow d\psi^*/dt < 0 \tag{14}$$

and the situations that lead to transformability are given by

$$\nu_g(t) > 0 \text{ and } dL'/dt < 0 \Rightarrow dW'/dt > 0 \Rightarrow d\psi^*/dt > 0 \tag{15}$$

$$\nu_g(t) < 0 \text{ and } dL'/dt > 0 \Rightarrow dW'/dt > 0 \Rightarrow d\psi^*/dt > 0 \tag{16}$$

Therefore, under certain global deformations, a Morph pattern in any hybrid state can potentially transform into other hybrid states on the kinematic branches of that system. In other words, the tessellated structure can switch between its kinematic branches of folding deformation by attaining the transition state. We refer to this ability of the Morph pattern as the reprogrammable morphing behavior.

4 Numerical Simulations Using Non-Linear Bar-and-Hinge Model

In this section, we perform numerical simulations to demonstrate the rigid transformability and the mode-locking behavior of the Morph origami assemblages.

4.1 Origami Mechanics Simulation. Although rigid folding behavior of origami structures is typically of interest, real structures are non-rigid and, therefore, it is important to verify the theoretical behavior of the Morph structure in the limit of panel rigidity by accurately simulating the mechanics. The mechanics of origami-based structures is typically simulated and studied using bar-and-hinge models [31]. Within the context of the numerical simulations, we assume that the panels are non-rigid, but we shall choose the model parameters in such a way that they almost behave as rigid. In this work, we use the simulation framework called MERLIN [25,32] to study the non-linear mechanics and the structural behavior of the Morph pattern undergoing finite deformation. This framework is built on the bar-and-hinge concept in which the entire origami structure is modeled as an enhanced truss-type structure comprising of *bars* which model the stretching deformations of the panels, and *hinges* or rotational springs which model the bending of the panels and folding of panels about the creases. In order to depict the rigid panel behavior, we choose the bending and stretching stiffness values of the springs and the bars to be seven and ten orders of magnitude more than the folding spring stiffness, respectively.

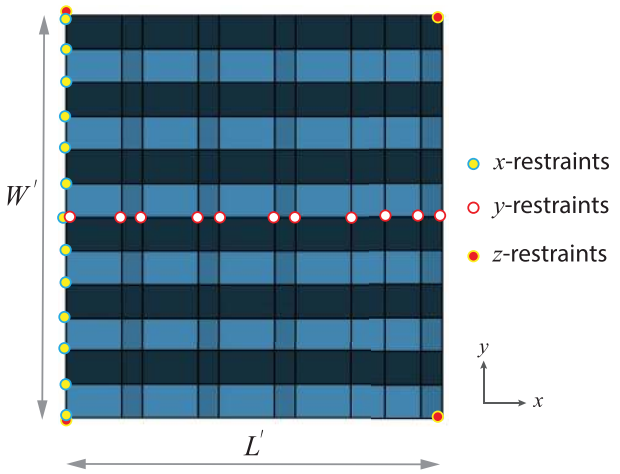

Fig. 10 Plan view of the hybrid Morph pattern with 6 × 6 cells showing the displacement restraints imposed on the nodes (vertices) for the numerical simulations

4.2 Numerical Uniaxial Experiments. To verify the rigid folding and the transformable/mode-locking behaviors of the Morph pattern we conduct numerical uniaxial experiments on two sample hybrid systems *EEEMME* and *MMMMME* (each with 6 × 6 cells), which have positive and negative global Poisson's ratios, respectively. The panel angles are chosen as $\alpha = 60$ deg and $\beta = 40$ deg, with dimensions $a = c = 1$. For both the systems, we impose displacement restraints as shown in Fig. 10 and the lateral load is applied along the L' direction at the free end. We consider a total of four experiments involving deformation: (1) Extension of *EEEMME* along the L' direction. (2) Contraction of *EEEMME* along the L' direction. (3) Extension of *MMMMME* along the L' direction. (4) Contraction of *MMMMME* along the L' direction. We seek to demonstrate the locking and transformable behavior of the systems based on arguments of local-global kinematics presented in Sec. 3.4.

4.3 Results and Discussion. The initial folded state of the two systems *MMMMME* and *EEEMME* is set to be $\psi = 60$ deg represented by points *A* and *B*, respectively in Fig. 11(*a*). Since *MMMMME* has a negative global Poisson's ratio, extension (contraction) of the L' dimension should lead to extension (contraction) of the W' dimension as well. Similarly, due to the global positive Poisson's ratio of *EEEMME*, extension (contraction) of the L' dimension should lead to contraction (extension) of the W' dimension. Figure 11(*a*) shows that the numerically calculated global dimensions during the uniaxial deformations of the two systems are in agreement with the theoretically predicted values.

The table of elastic energy distribution shown in Fig. 11(*b*) demonstrates that the deformations are primarily driven by folding about the creases with almost no influence of bending and stretching of panels. This shows that the Morph pattern is able to transform from an arbitrary folded state (say *A* or *B*) to the transition state (*T* in Fig. 11(*a*)) or extreme folded states (*C* or *D* in Fig. 11(*a*)), through rigid folding alone. Once any hybrid Morph system transforms to a transition state, it can virtually transform into any of the other feasible hybrid states (see Fig. 6). Since the folding

(*a*)

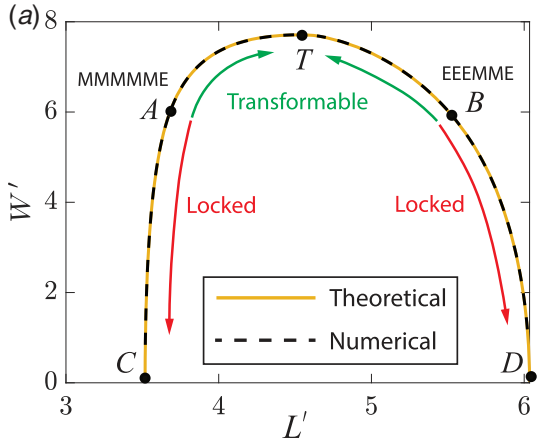

(*b*)

	Folding Energy	Bending Energy	Stretching Energy
EEEMME extension	99.9992%	0.0002%	0.0006%
EEEMME contraction	99.9825%	0.0165%	0.0010%
MMMMME extension	99.9810%	0.0180%	0.0010%
MMMMME contraction	99.9837%	0.0049%	0.0115%

Fig. 11 (*a*) Theoretical and numerical comparison of the configuration path of the *MMMMME* and *EEEMME* hybrid patterns. The initial folded states of *MMMMME* and *EEEMME* patterns are represented by points *A* and *B*, respectively, on the configuration path. The points *C*, *D* represent the extreme folded states and *T* represents the transition state. (*b*) Various components of the elastic energy stored in the hybrid origami system corresponding to the point of maximum energy over the total deformation range.

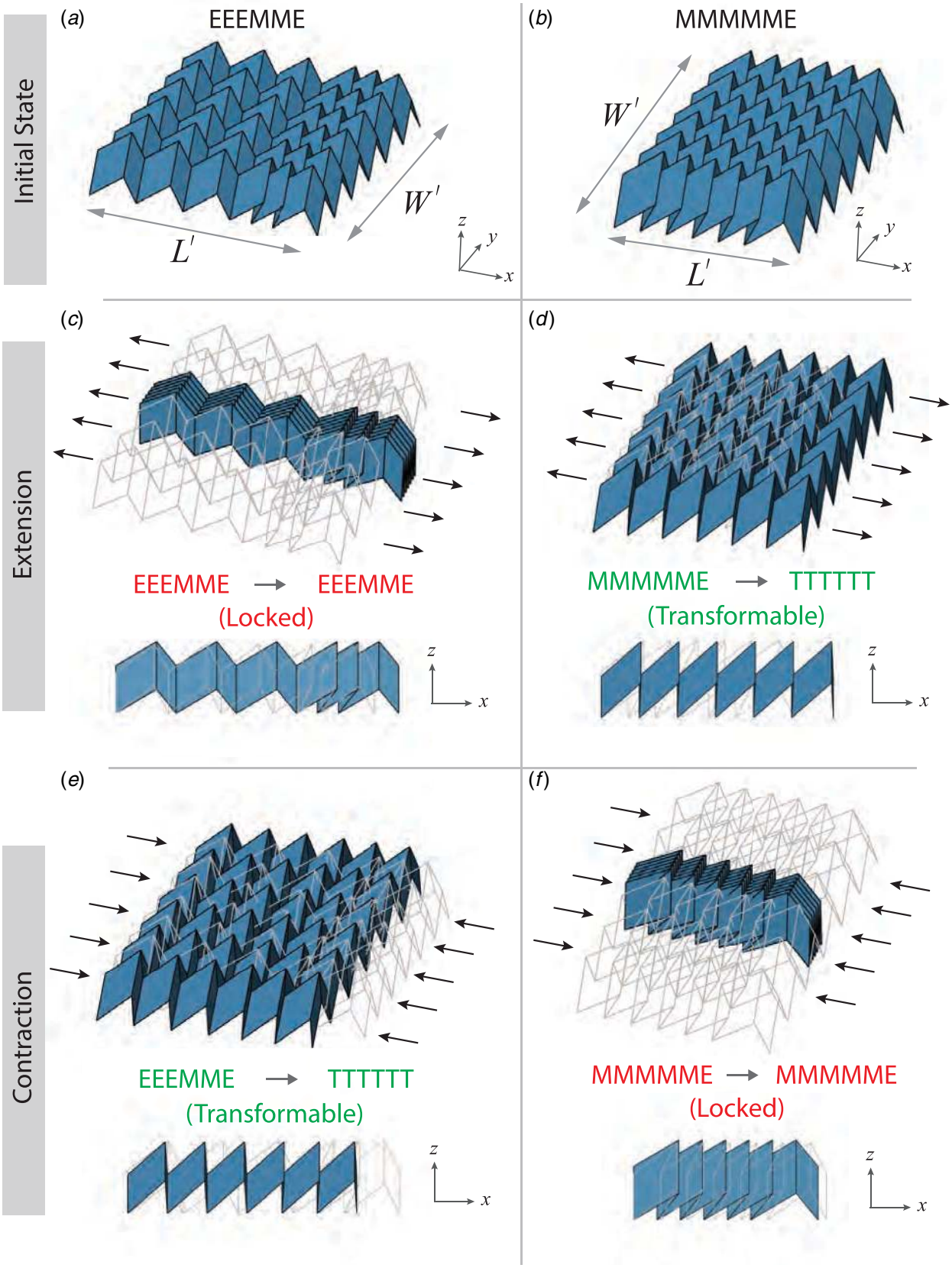

Fig. 12 Numerical simulation of the uniaxial deformation of the hybrid Morph patterns. (*a*), (*b*) Initial folded state of the ***EEEMME*** and ***MMMMME*** patterns. (*c*), (*d*) Final deformed state due to extension of the two patterns leading to locked and transformable configurations for ***EEEMME*** and ***MMMMME***, respectively. (*e*), (*f*) Final deformed state due to contraction of the two patterns leading to transformable and locked configurations for ***EEEMME*** and ***MMMMME***, respectively. In (*c*)–(*f*), the line structures represent the initial folded states shown in (*a*) and (*b*).

deformations are reversible, it can be shown that the Morph pattern is inter-transformable among all of its hybrid states through rigid folding.

Figure 12 shows the initial and final folded states of the *EEEMME* and *MMMMME* hybrid Morph systems during the uniaxial deformations. The results verify that it is possible to either lock the cells of a hybrid Morph pattern within their configuration or to transform them into the transition state depending on the type of loading (tension/compression) applied on the system. Moreover, the behavior of a hybrid system with globally positive Poisson's ratio is exactly opposite to that of the system with globally negative Poisson's in terms of the cells being transformable or locked in their original vertex topology.

From the above discussion on Figs. 11 and 12, we can say that the hybrid Morph system is capable of undergoing rigid kinematic folding toward a transition state when subjected to extension or contraction (in the L' direction) depending on whether the global Poisson's ratio is negative or positive, respectively. Since the transition state is a kinematic bifurcation point (see Fig. 7), the system can access any of the kinematic branches for further folding from that configuration. Therefore, the tessellated Morph structure is characterized by reprogrammable kinematic branches as it can potentially be made to switch between its branches in the parameter space.

5 Conclusion

We discussed the Morph pattern, and provided detailed explanations to the intriguing features of the two-dimensional tessellations. We showed that the Morph unit cells can be combined to form either uniform or hybrid states of the Morph pattern. Further, we explained how these states are inter-transformable through rigid origami kinematics. We also proposed a new way to describe and distinguish various configuration paths of the Morph pattern. Finally, we derived the conditions for switching the sign of Poisson's ratio of the Morph pattern and explained the mode-locking/transformability features. We presented numerical simulations based on non-linear origami mechanics to verify the theoretically predicted mechanical behavior of the hybrid Morph pattern.

5.1 Future Directions. We foresee applications of the rigid-foldable Morph pattern in terms of the ability to control (i) geometry or spatial appearance of a system and (ii) "material" distribution in a system. The former is related to the arrangement of the strips in different modes that could be useful in morphing structures for architectural or camouflage purposes. Since, the geometric arrangement also modifies the symmetry in a system, we think that it could be useful in topological metamaterials, which heavily depend on symmetry manipulation [33,34]. The latter aspect on material distribution has a much broader scope. The Eggbox and Miura modes have contrasting mechanical properties (e.g., oppositely signed Poisson's ratios) and the Morph pattern has the kinematic ability to re-distribute the strips of these modes in an arbitrary manner and therefore can act as a *designer material*. Lattice systems with such a feature could be useful as acoustic metamaterials [6]. Physical realization of the Morph pattern and its reprogrammable morphing abilities could be pursued through advanced 3D printing techniques [35] and smart materials. In the current paper, the reprogramming is achieved by manual operation. However, in the future, this can be achieved, for example, using multiple stimuli-responsive materials [36,37] at the hinges, so that different external stimuli would trigger folding into different branches.

Acknowledgment

We acknowledge support from the National Science Foundation (NSF) through grant CMMI 1538830, and from the endowment provided by the Raymond Allen Jones Chair at the Georgia Institute of Technology. PPP acknowledges the support from the Indian Institute of Technology Madras and the Science & Engineering Research Board (SERB) of the Department of Science & Technology, Government of India, through award SRG/2019/000999. SPV acknowledges the support from the fellowship offered by Prime Minister's Research Fellows (PMRF) Scheme, Ministry of Human Resource Development, Government of India. The information provided in this paper is the sole opinion of the authors and does not necessarily reflect the views of the sponsors or sponsoring agencies.

Conflict of Interest

There are no conflicts of interest.

Data Availability Statement

The datasets generated and supporting the findings of this article are obtainable from the corresponding author upon reasonable request.

References

[1] Silverberg, J. L., Evans, A. A., McLeod, L., Hayward, R. C., Hull, T., Santangelo, C. D., and Cohen, I., 2014, "Using Origami Design Principles to Fold Reprogrammable Mechanical Metamaterials," Science, **345**(6197), pp. 647–650.
[2] Li, S., Fang, H., and Wang, K., 2016, "Recoverable and Programmable Collapse From Folding Pressurized Origami Cellular Solids," Phys. Rev. Lett., **117**(11), p. 114301.
[3] Dudte, L. H., Vouga, E., Tachi, T., and Mahadevan, L., 2016, "Programming Curvature Using Origami Tessellations," Nat. Mater., **15**(5), p. 583.
[4] Overvelde, J. T., Weaver, J. C., Hoberman, C., and Bertoldi, K., 2017, "Rational Design of Reconfigurable Prismatic Architected Materials," Nature, **541**(7637), p. 347.
[5] Boatti, E., Vasios, N., and Bertoldi, K., 2017, "Origami Metamaterials for Tunable Thermal Expansion," Adv. Mater., **29**(26), p. 1700360.
[6] Pratapa, P. P., Suryanarayana, P., and Paulino, G. H., 2018, "Bloch Wave Framework for Structures With Nonlocal Interactions: Application to the Design of Origami Acoustic Metamaterials," J. Mech. Phys. Solids., **118**, pp. 115–132.
[7] Schenk, M., Guest, S., and McShane, G., 2014, "Novel Stacked Folded Cores for Blast-Resistant Sandwich Beams," Int. J. Solids. Struct., **51**(25), pp. 4196–4214.
[8] Gattas, J. M., and You, Z., 2015, "The Behaviour of Curved-Crease Foldcores Under Low-Velocity Impact Loads," Int. J. Solids. Struct., **53**, pp. 80–91.
[9] Filipov, E. T., Tachi, T., and Paulino, G. H., 2015, "Origami Tubes Assembled Into Stiff, Yet Reconfigurable Structures and Metamaterials," Proc. Natl. Acad. Sci. U.S.A., **112**(40), pp. 12321–12326.
[10] Fang, H., Li, S., and Wang, K. W., 2016, "Self-Locking Degree-4 Vertex Origami Structures," Proc. R. Soc. - A, **472**(2195), p. 20160682.
[11] Liu, K., Tachi, T., and Paulino, G. H., 2019, "Invariant and Smooth Limit of Discrete Geometry Folded From Bistable Origami Leading to Multistable Metasurfaces," Nat. Commun., **10**(1), pp. 1–10.
[12] Schenk, M., and Guest, S. D., 2013, "Geometry of Miura-Folded Metamaterials," Proc. Natl. Acad. Sci. U.S.A., **110**(9), pp. 3276–3281.
[13] Wei, Z. Y., Guo, Z. V., Dudte, L., Liang, H. Y., and Mahadevan, L., 2013, "Geometric Mechanics of Periodic Pleated Origami," Phys. Rev. Lett., **110**(21), p. 215501.
[14] Nassar, H., Lebée, A., and Monasse, L., 2017, "Curvature, Metric and Parametrization of Origami Tessellations: Theory and Application to the Eggbox Pattern," Proc. R. Soc. - A, **473**(2197), p. 20160705.
[15] Schenk, M., 2012, "Folded Shell Structures," Ph.D. thesis, University of Cambridge.
[16] Waitukaitis, S., Menaut, R., Chen, B. G.-g., and van Hecke, M., 2015, "Origami Multistability: From Single Vertices to Metasheets," Phys. Rev. Lett., **114**(5), p. 055503.
[17] Fang, H., Li, S., Ji, H., and Wang, K., 2016, "Uncovering the Deformation Mechanisms of Origami Metamaterials by Introducing Generic Degree-four Vertices," Phys. Rev. E, **94**(4), p. 043002.
[18] Pratapa, P. P., Liu, K., and Paulino, G. H., 2019, "Geometric Mechanics of Origami Patterns Exhibiting Poisson's Ratio Switch by Breaking Mountain and Valley Assignment," Phys. Rev. Lett., **122**(15), p. 155501.
[19] Ho, D. T., Park, S. -D., Kwon, S. -Y., Park, K., and Kim, S. Y., 2014, "Negative Poisson's Ratios in Metal Nanoplates," Nat. Commun., **5**, p. 3255.
[20] Rafsanjani, A., and Pasini, D., 2016, "Bistable Auxetic Mechanical Metamaterials Inspired by Ancient Geometric Motifs," Extreme Mech. Lett., **9**(2), pp. 291–296.
[21] Liu, J., and Zhang, Y., 2018, "Soft Network Materials With Isotropic Negative Poisson's Ratios Over Large Strains," Soft. Matter., **14**(5), pp. 693–703.
[22] Yasuda, H., and Yang, J., 2015, "Reentrant Origami-Based Metamaterials With Negative Poisson's Ratio and Bistability," Phys. Rev. Lett., **114**(18), p. 185502.

[23] Rafsanjani, A., and Bertoldi, K., 2017, "Buckling-Induced Kirigami," Phys. Rev. Lett., **118**(8), p. 084301.
[24] Yang, N., and Silverberg, J. L., 2017, "Decoupling Local Mechanics From Large-Scale Structure in Modular Metamaterials," Proc. Natl. Acad. Sci. U.S.A., **114**(14), pp. 3590–3595.
[25] Liu, K., and Paulino, G. H., 2017, "Nonlinear Mechanics of Non-Rigid Origami: An Efficient Computational Approach," Proc. R. Soc. A: Math., Phys. Eng. Sci., **473**(2206), p. 20170348.
[26] You, Z., and Chen, Y., 2011, *Motion Structures: Deployable Structural Assemblies of Mechanisms*, CRC Press, Boca Raton, FL.
[27] Lang, R. J., 2017, *Twists, Tilings, and Tessellations: Mathematical Methods for Geometric Origami*, AK Peters/CRC Press, Boca Raton, FL.
[28] Sussman, G. J., and Wisdom, J., 2015, *Structure and Interpretation of Classical Mechanics*, The MIT Press, Cambridge, MA.
[29] Liu, C., and Felton, S. M., 2018, "Transformation Dynamics in Origami," Phys. Rev. Lett., **121**(25), p. 254101.
[30] Chen, B. G.-g., and Santangelo, C. D., 2018, "Branches of Triangulated Origami Near the Unfolded State," Phys. Rev. X, **8**(1), p. 011034.
[31] Filipov, E. T., Liu, K., Tachi, T., Schenk, M., and Paulino, G. H., 2017, "Bar and Hinge Models for Scalable Analysis of Origami," Int. J. Solids. Struct., **124**, pp. 26–45.
[32] Liu, K., and Paulino, G. H., 2018, "Highly Efficient Nonlinear Structural Analysis of Origami Assemblages Using the MERLIN2 Software," Origami, **7**, pp. 1167–1182.
[33] Chen, B. G.-g., Liu, B., Evans, A. A., Paulose, J., Cohen, I., Vitelli, V., and Santangelo, C., 2016, "Topological Mechanics of Origami and Kirigami," Phys. Rev. Lett., **116**(13), p. 135501.
[34] Rocklin, D. Z., Zhou, S., Sun, K., and Mao, X., 2017, "Transformable Topological Mechanical Metamaterials," Nat. Commun., **8**, p. 14201.
[35] Zhao, Z., Kuang, X., Wu, J., Zhang, Q., Paulino, G. H., Qi, H. J., and Fang, D., 2018, "3D Printing of Complex Origami Assemblages for Reconfigurable Structures," Soft. Matter., **14**(39), pp. 8051–8059.
[36] Mao, Y., Yu, K., Isakov, M. S., Wu, J., Dunn, M. L., and Qi, H. J., 2015, "Sequential Self-Folding Structures by 3D Printed Digital Shape Memory Polymers," Sci. Rep., **5**, p. 13616.
[37] Hu, L., Wan, Y., Zhang, Q., and Serpe, M. J., 2020, "Harnessing the Power of Stimuli-Responsive Polymers for Actuation," Adv. Funct. Mater., **30**(2), p. 1903471.